Journal of the Nigerian Association of Mathematical Physics
Volume 51 (*May, 2019 Issue*), pp187 – 198
© *J. of NAMP*

PROTON SCATTERING FROM ^{40,48,60}CA USING HOROWITZ-LOVE-FRANEY MODEL

YAHYA Wasiu Akanni

Department of Physics and Materials Science, Kwara State University, Malete, Kwara State, Nigeria.

Abstract

The study of unstable nuclei have been made possible with the availability of radioactive ion beam facilities. There is therefore the need to test existing theories in Nuclear Physics and to develop new ones where existing theories fail to describe the scattering observables for scattering from these unstable nuclei. In this work, proton elastic scattering from some calcium isotopes has been studied using microscopic formalisms. The scattering observables have been computed using Horowitz-Love-Franey (HLF) and the original relativistic impulse approximation (IA1) formalisms with the target densities obtained from relativistic mean–field theory Lagrangian. We showed that the original relativistic impulse approximation formalism was able to successfully describe the elastic scattering observables only at $T_{lab} \geq 400$ MeV, while the HLF formalism gave correct descriptions of the observables at lower incident laboratory energies. We have employed two models to calculate the relativistic mean-field (RMF) densities viz.: DDPC1 and DDME2. We find that the two RMF models were able to successfully describe the scattering observables when compared with available experimental data. Finally for $p+^{60}Ca$ where there is no experimental data for now, we compared our calculations with the results obtained using global Dirac optical model phenomenology.

1. Introduction

The study of electron and proton scattering from neutron rich nuclei have been made possible with the availability of radioactive ion beams (RIB). This will serve as a test for the existing nuclear physics theories. Surprising results have so far been obtained such as the appearance of new magic numbers, new regions of deformation, the disappearance of the normal shell closures observed near the stability valley, and nuclear halos and skins [1, 2]. The RIB facilities will make large amount of neutron rich nuclei data available, and will enhance the study of the exotic nuclei via electron and proton scattering. One can obtain information on the ground state neutron density and transition density distributions with proton and electron scattering [3]. Due to its larger mean free path in the nuclear medium, proton elastic scattering is a good tool to probe neutron density distributions at intermediate energy (200 - 500 MeV). Experiments involving proton scattering on exotic nuclei are often performed in inverse kinematics due to the short lifetime of unstable nuclei. In this case, the heavy particle (nucleus to study) is accelerated, and the light particle (in our case proton) serves as the target.

The study of proton elastic scattering from $^{120,132}Sn$ and $^{40,48,60}Ca$ have been studied using generalised impulse approximation (IA2) with densities obtained from NL3 and FSUGold Lagrangians [1, 4]. Unexpectedly large charge radii in neutron-rich calcium isotopes has also been studied [5]. There is the renewed interest in the study of neutron-rich calcium isotopes in recent times.

In [6], elastic proton scattering from proton-rich ^{30}S and ^{34}Ar isotopes at 53 MeV/A and 47MeV/A have been studied. Angular distributions of proton elastic scattering at 277–300 MeV per nucleon on ^{9}C has

Corresponding Author**:** Yahaya W.A., Email: wasiu.yahya@gmail.com , Tel: +2348036289110

also been studied in [7], where the experiment was also performed in inverse kinematics. [8] also presents a study of proton scattering from ^{6}He, ^{8}He, ^{6}Li, ^{8}Li, ^{9}Li and ^{11}Li at intermediate energies. Theoretical calculations for proton scattering from unstable nuclei have been carried out in [1] and [9].

In this paper, we present the study of elastic proton scattering from ^{40,48,58,60}Ca nuclei at intermediate energies using HLF and IA1 formalisms. We have used nuclear densities obtained from relativistic mean field theory bound state wave-functions with the DDME2 and DDPC1 parameter sets. The outline of the paper is given as follows. In Section 2, we present the formalisms of the original relativistic impulse approximation and Horowitz-Love-Franey model. Section 3 contains results of the elastic scattering observables namely the differential cross section and analysing power, which are calculated by solving the Dirac equation with relativistic optical potentials. The conclusion is given in Section 4.

2 Formalism

2.1 Relativistic Impulse Approximation (IA1)

For proton–nucleus scattering, the Dirac equation is written in the relativistic impulse approximation model as:

$$[-i\alpha\cdot\nabla + V(r,E) + \beta(M + S(r,E)) + V_C]\psi = E\psi, \quad (1)$$

where α and β are 4×4 Dirac matrices which act on the projectile wave function, $S(r,E)$ and $V(r,E)$ are, respectively, the scalar and vector potentials, V_C is the Coulomb potential, and E is the centre of mass energy. The optical potential in the relativistic impulse approximation (IA1) is calculated by folding the NN invariant scalar and vector amplitudes with the target scalar and vector densities, respectively; the contribution of the tensor optical potential is very small [2, 10]. The IA1 uses the Dirac equation to describe the motion of the projectile in the field of the target nucleus. In [10], it was found that the IA1 differential cross sections were too large and the analysing powers too small at energies 181 MeV and 300 MeV. However, at 400 MeV the results agreed well with experimental data, and it was found that the best agreement was at 500 MeV. They found that the original IA1 predictions were satisfactory at energies above 400 MeV. At low energy, however, where nuclear-medium effects are important, the IA1 results were too large. To apply IA1 to lower energies, modifications due to exchange and Pauli-blocking effects have to be included [11, 12].

In [13], the authors studied the use of proton elastic scattering at high and intermediate energies to extract information about density distributions of unstable nuclei using relativistic impulse approximation (IA1) and Glaubal model for proton scattering. They found that the IA1 was able to better describe the spin observables of the unstable nuclei (they studied) than the Glauber model.

The first–order optical potential in the IA1 formalism is given as

$$U^{(1)}(q) = -\frac{4\pi ik}{m}\sum_{\beta}\sum_{i=1}^{A}\langle\widetilde{\Phi}_0|\hat{\mathcal{F}}\ |\widetilde{\Phi}_0\rangle. \quad (2)$$

Here $\widetilde{\Phi}_0$ denotes a relativistic Hartree-Fock or relativistic mean field bound state wave function for the target nucleus, k is the p-A centre-of-mass frame three-momentum, m is the projectile mass, and the momentum transfer

$$\mathbf{q} = \mathbf{k} - \mathbf{k}'. \quad (3)$$

The ground state wave function is typically a Hartree product of single–particle four component wave function ϕ_α, with the states labelled α. The sums over α run over all the occupied single-particle states in the nucleus. The relativistic Lorentz invariant NN amplitude in the IA1 formalism are given by [11, 16, 17]:

$$\hat{\mathcal{F}} = \mathcal{F}_S\,(\mathbb{I}_4\otimes\mathbb{I}_4) + \mathcal{F}_P\,(\gamma^5_{(1)}\otimes\gamma^5_{(2)}) + \mathcal{F}_V\,(\gamma^\mu_{(1)}\otimes\gamma_{(2)\,\mu})$$
$$+\mathcal{F}_A\,(\gamma^5_{(1)}\gamma^\mu_{(1)}\otimes\gamma^5_{(2)}\gamma_{(2)\,\mu}) + \mathcal{F}_T\,(\sigma_1^{\mu\nu}\otimes\sigma_{(2)\,\mu\nu}), \quad (4)$$

or in the short form

$$\hat{\mathcal{F}}(s,t) = \sum_\beta \mathcal{F}_\beta\lambda^\beta\otimes\lambda_\beta. \quad (5)$$

The subscripts "1" and "2" indicate the action on the projectile (proton) and target nucleus, respectively. The five complex amplitudes for scalar (S), vector (V), tensor (T), pseudoscalar (P), and axial vector (A) interactions are determined directly from the NN phase shifts which parametrize the physical NN scattering data [16]. They depend on the square of the momentum transfer q^2 and the Mandelstam invariant parameter s. The relativistic (IA1) NN invariant amplitudes used in this work are those described in [16].

As explained in [18], for a spin-saturated nucleus, the matrix element involves a trace over struck-nucleon spins which eliminates all but the scalar (F_S), time component of vector ($\gamma^0 F_V$) terms and a small tensor term from the Dirac scattering amplitude shown above. The optical potential takes care of the multiple-scattering effect. The first-order optical potential in the IA1 formalism is then given as:

$$U^{(1)}(q) = -\frac{4\pi ik}{m}[F_S(q)\rho_S(q) + \gamma^0 F_V(q)\rho_V(q) - 2i\alpha_1 \cdot \hat{r}F_T(q)\rho_T(q)], \quad (6)$$

where the scalar, vector, and tensor form factors are given, respectively, by

$$\rho_S(q) = 4\pi \int_0^\infty r^2 j_0(qr)\rho_S(r)dr, \quad (7)$$

$$\rho_V(q) = 4\pi \int_0^\infty r^2 j_0(qr)\rho_V(r)dr, \quad (8)$$

$$\rho_T(q) = 4\pi \int_0^\infty r^2 j_1(qr)\rho_T(r)dr. \quad (9)$$

Here, j_0 and j_1 are the spherical Bessel function of the first kind, and the scalar, vector, and tensor densities are given by

$$\rho_S(r) = \sum_\alpha^{occ} \left(\frac{2j_\alpha+1}{4\pi r^2}\right)[g_\alpha^2(r) - f_\alpha^2(r)], \quad (10)$$

$$\rho_V(r) = \sum_\alpha^{occ} \left(\frac{2j_\alpha+1}{4\pi r^2}\right)[g_\alpha^2(r) + f_\alpha^2(r)], \quad (11)$$

$$\rho_T(r) = \sum_\alpha^{occ} \left(\frac{2j_\alpha+1}{4\pi r^2}\right)2g_\alpha(r)f_\alpha(r), \quad (12)$$

where the sums run over all the occupied single-particle states in the nucleus. The on–shell $t\rho$ form of the IA1 optical potential in coordinate space is obtained from the Fourier transform of the momentum space optical potential given in equation (6) as:

$$U^{(1)}(r) = S(r) + \gamma_1^0 V(r) - 2i\alpha_1 \cdot \hat{r}T(r), \quad (13)$$

where the subscript "1" in α_1 and γ_1^0 indicates that both act on the incident proton and the coordinate space scalar (S(r)), vector (V(r)), and tensor (T(r)) IA1 optical potentials are given, respectively, by [15]

$$S(r) = -\frac{4\pi ik}{m}\sum_{t=p,n}\frac{1}{2\pi^2}\int_0^\infty dq q^2 j_0(qr)\ \mathcal{F}_{t,S}(q)\ \rho_{t,S}(q), \quad (14)$$

$$V(r) = -\frac{4\pi ik}{m}\sum_{t=p,n}\frac{1}{2\pi^2}\int_0^\infty dq q^2 j_0(qr)\ \mathcal{F}_{t,V}(q)\ \rho_{t,V}(q), \quad (15)$$

$$T(r) = -\frac{4\pi ik}{m}\sum_{t=p,n}\frac{1}{2\pi^2}\left[r\int_0^\infty dq q^2 j_0(qr)\ \mathcal{F}_{t,T}(q)\ \rho_{t,T}(q) + \int_0^\infty dq q^2 j_1(qr)\ \frac{d\mathcal{F}_{t,T}(q)}{dq}\rho_{t,T}(q)\right]. \quad (16)$$

In the IA1 formalism, the Schrödinger equivalent central and spin orbit potentials required to solve the coordinate space Dirac equation (in order to obtain the scattering observables) are written as

$$U_{\rm c}(r) = \frac{1}{2E}[2mS(r) + 2EV(r) + S^2(r) - V^2(r) - 2V_cV(r) + \left(T^2 - \frac{T}{A}\frac{dA}{dr} + \frac{2T}{r} + \frac{dT}{dr}\right) + 2EU_{\rm Darwin}\Big], \quad (17)$$

and

$$U_{\rm so}(r) = \frac{1}{2E}\left(-\frac{1}{rA}\frac{dA}{dr} + \frac{2T}{r}\right), \quad (18)$$

where

$$U_{\rm Darwin}(r) = \frac{1}{2E}\left[-\frac{1}{2r^2A}\frac{d}{dr}\left(r^2\frac{dA}{dr}\right) + \frac{3}{4A^2}\left(\frac{dA}{dr}\right)^2\right] \quad (19)$$

and

$$A(r) = \frac{1}{E+m}(m + S(r) + E - V(r) - V_c), \quad (20)$$

V_c is the Coulomb potential and m is the mass of the projectile.

2.2 Horowitz-Love-Franey (HLF) model

We give here a brief description of the Horowitz-Love-Franey model (also referred to as Relativistic Love-Franey model). A detailed description has been given in [12, 17] and references therein. In this model, the

relativistic Lorentz-invariant amplitudes $\mathcal{F}^L(q,E)$ have both direct and exchange terms, that is

$$\mathcal{F}^L(q,E) = \frac{iM^2}{2E_C k_c}[F_D^L(q) + F_{EX}^L(Q)], \quad (21)$$

where

$$F_D^L(q) = \sum_{i=1}^{N} \delta_{L,L(i)}\{\tau_1 \cdot \tau_2\}^{I_i} f^i(q), \quad (22)$$

$$F_{EX}^L(q) = (-1)^T \sum_{i=1}^{N} C_{L(i),L}\{\tau_1 \cdot \tau_2\}^{I_i} f^i(Q). \quad (23)$$

q denotes the magnitude of the direct three-momentum transfer, and Q is the magnitude of the exchange-momentum transfer, $I_i = (0,1)$ is the isospin of the ith meson, T denotes the total isospin of the two-nucleon system, $\{\tau_1 \cdot \tau_2\}^{I_i}$ is 1 or -3 for different T and I_i Also $C_{L(i),L}$ is the Fierz matrix [19] and

$$f^i(x) = \frac{g_i^2}{x^2+m_i^2}\left(1+\frac{x^2}{\Lambda_i^2}\right)^{-2} - i\frac{\bar{g}_i^2}{x^2+\bar{m}_i^2}\left(1+\frac{x^2}{\bar{\Lambda}_i^2}\right)^{-2}. \quad (24)$$

Here x represents either q or Q, $(g_i^2, \bar{g}_i^2)$, $(m_i, \bar{m}_i)$, and $(\Lambda_i, \bar{\Lambda}_i)$ denote the real and imaginary parts of the coupling constant, mass, and cut-off parameter of the ith meson. The above parameters are obtained by fitting the calculated amplitudes with the values extracted from the NN scattering data. Detailed descriptions of this formalism can be found in [12]. The NN scattering data have also been given in [11].

3. Results and Discussion

The results of the calculations are given in this section. Table 1 shows the results of the charge radii (r_{ch}) computed using DDPC1, DDME2, and FSUGold relativistic mean field (RMF) parametrizations. The DDPC1 and DDME2 models are described in [20] while FSUGold model was first presented in [21]. The calculated radii using FSUGold parametrization have been taken from [1] and [2]. The calculations of the FSUGold parametrization have been included for comparison purpose. When compared with available experimental data (for ^{40,48}Ca), one observes that three models give very good descriptions of the radii for ^{40,48}Ca. The FSUGold model gives the best description for the charge radius of ^{40}Ca, while DDME2 model gives the best description for charge radius of ^{48}Ca. We believe that there are plans to measure the charge radii of neutron-rich Calcium isotopes [5]. When the results of measurements become available, one will be able to determine the model which gives the best results.

Table 1: Charge radii for calcium isotopes calculated using relativistic mean field theory with the DDME2, DDPC1, and FSUGold parametrizations.

Nucleus	Observable	DDME2	DDPC1	FSUGold	Experiment
^{40}Ca	r_{ch}	3.464323	3.456533	3.4795	3.4776 [22]
^{48}Ca	r_{ch}	3.481498	3.489492	3.4597	3.4771 [22]
^{54}Ca	r_{ch}	3.565427	3.556354	3.5741	
^{58}Ca	r_{ch}	3.629128	3.616640	3.6089	
^{60}Ca	r_{ch}	3.659942	3.646342	3.6300	

3.1 Koning-Delaroche model and Global Dirac Phenomenology

Here, we compare the results of the scattering observables calculated using Koning-Delaroche model [23] (implemented in the TALYS package) and using the global Dirac phenomenology described in [2, 24, 25]. The Koning-Delaroche model is a non-relativistic phenomenological optical model presented in [23]. It was formulated to describe nucleon-nucleus scattering from 1keV up to 200 MeV. The model was later extended in order to be able to predict the total, elastic and non-elastic cross sections up to 1 GeV [26]. We want to verify the use of the extended model for incident energies greater than 200 MeV.

The scattering observables are calculated, in the Koning-Delaroche model (KD03) [23], by substituting the non-relativistic central and spin-orbit optical potentials into the Schrödinger equation, which is then numerically solved. In the global Dirac phenomenology (DP), the scattering observables are obtained by numerically solving the coordinate-space Dirac equation. Figures 1 through 4 show the plots of the differential scattering cross-section and analysing power obtained using both the KD03 and DP models for proton scattering from ^{40}Ca at incident energies T_{lab} = 65,100,200,500MeV. In these figures, the differential cross-section plots are shown on the left while the analysing power plots are shown on the right.

The DP model results are shown in solid lines while the KD03 model results are shown in dashed lines. The experimental data are shown in circles.

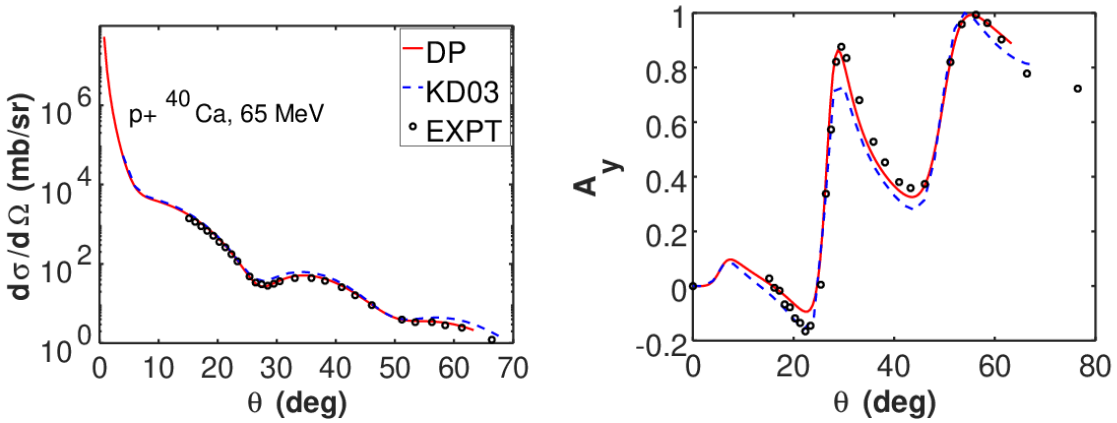

Figure 1: Differential cross-section and analysing power plots for proton scattering from ^{40}Caat $T_{lab} =$ 65MeV. The DP model results are shown in solid lines while the KD03 model results are shown in dashed lines. The experimental data are shown in circles.

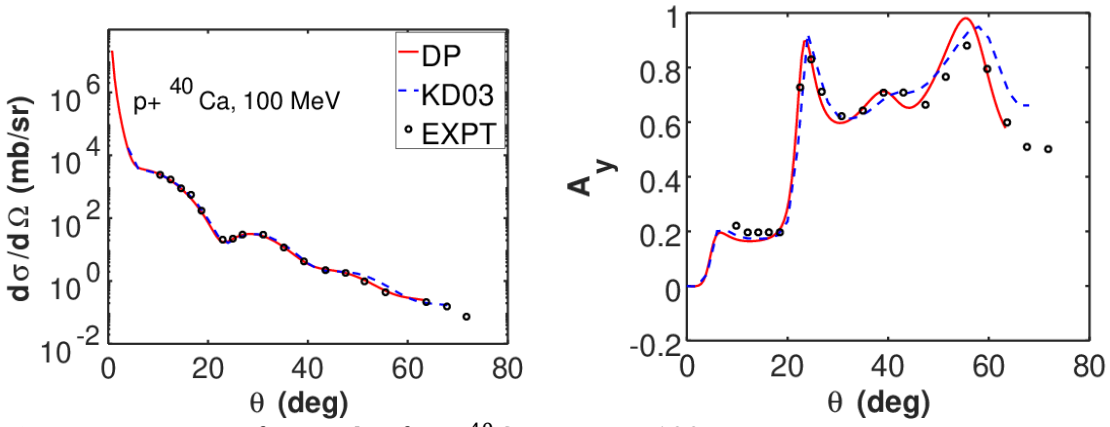

Figure 2: Same as in figure 1 but for ^{40}Ca at $T_{lab} = 100$MeV.

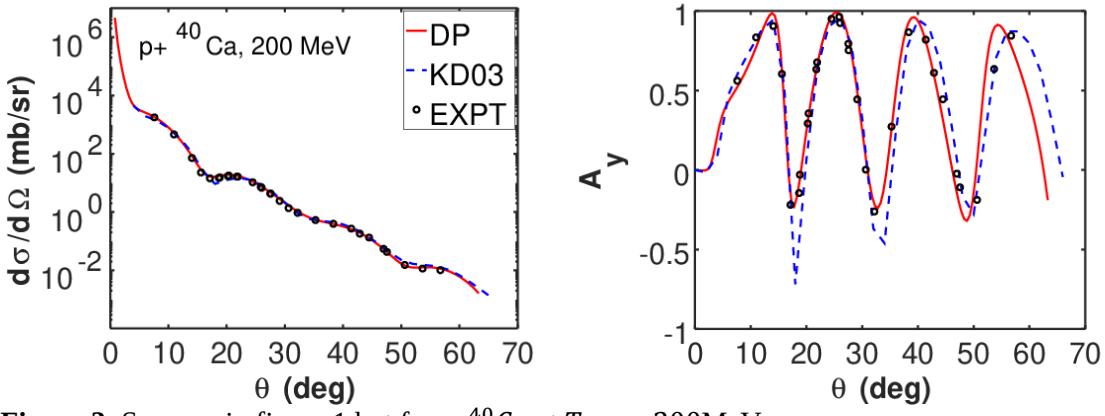

Figure 3: Same as in figure 1 but for ^{40}Ca at $T_{lab} = 200$MeV.

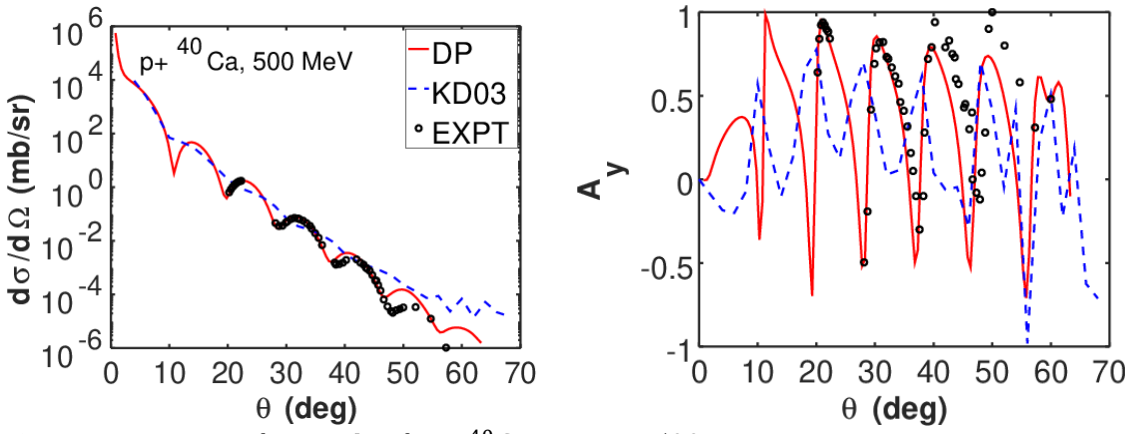

Figure 4: Same as in figure 1 but for ^{40}Ca at $T_{lab} = 500$MeV.

One can observe from the figures that both Koning-Delaroche (KD03) and global Dirac phenomenology (DP) models describe successfully the scattering observables at $T_{lab} = 65{,}100{,}200$ MeV. But at $T_{lab} = 500$MeV, only the DP model successfully describes the scattering observables; the KD03 model could not. This means that the KD03 model should not be used to calculate differential cross-section and analysing power for incident energies greater than 200 MeV.

3.2 IA1 formalism using DDME2 and DDPC1 energy functionals

The results of the scattering observables calculated using the IA1 formalism with the densities obtained using DDPC1 and DDME2 functionals are presented here. The DDME2 and DDPC1 functionals were presented in [20]. Figures 5 through 8 show the plots of the differential cross-section and analysing power calculated for proton scattering from ^{48}Ca using IA1 formalism with the DDPC1 and DDME2 Lagrangians for incident projectile energies $T_{lab} = 200, 318, 500, 800$MeV. The results of the calculations using IA1 formalism with the DDPC1 and DDME2 are shown in solid and dashed lines, respectively. The DP results are shown in dotted lines while experimental data are shown in circles.

One can observe from figures 5 through 8 that the IA1 formalism successfully describes the scattering observables at $T_{lab} = 500$ and 800MeV, but could not accurately describe the scattering observables at $T_{lab} = 200$ and 318 MeV. This has been attributed to the large scalar and vector optical potentials produced by the IA1 formalism at energies lower than 400MeV. See also [1, 2] for detailed explanations. What we learn from these results is that even with the densities obtained using new energy functionals, the IA1 formalism could not successfully describe the scattering observables at energies lower than 400 MeV.

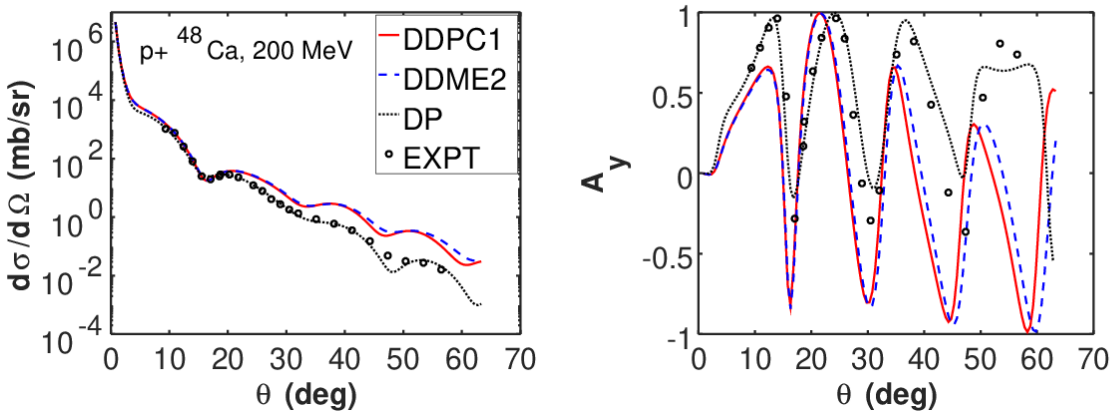

Figure 5: Differential cross-section and analysing power plots for proton scattering from ^{48}Ca at $T_{lab} = 200$ MeV using IA1 formalism with the DDPC1 and DDME2 functionals. The results of the calculations using IA1 formalism with the DDPC1 and DDME2 are shown in solid and dashed lines, respectively. The DP results are shown in dotted lines while experimental data are shown in circles.

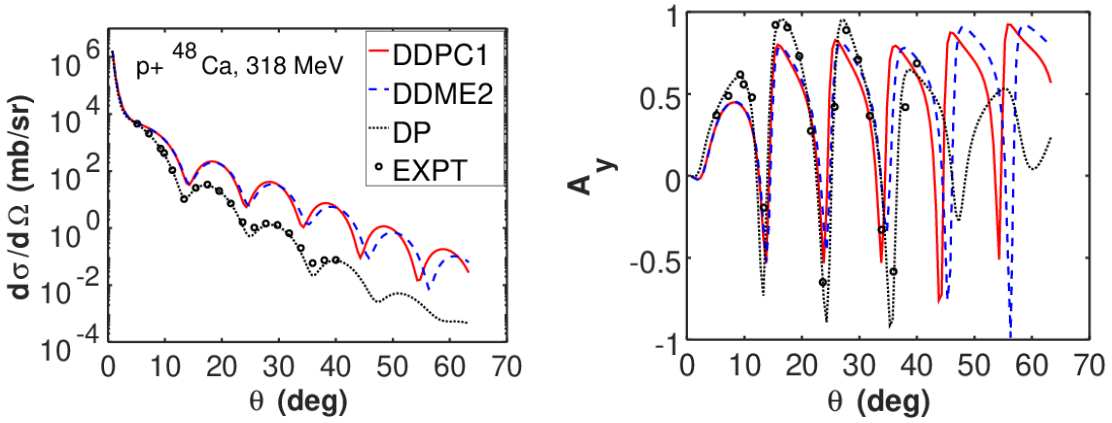

Figure 6: Same as in figure 5 but for $T_{lab} = 318$MeV.

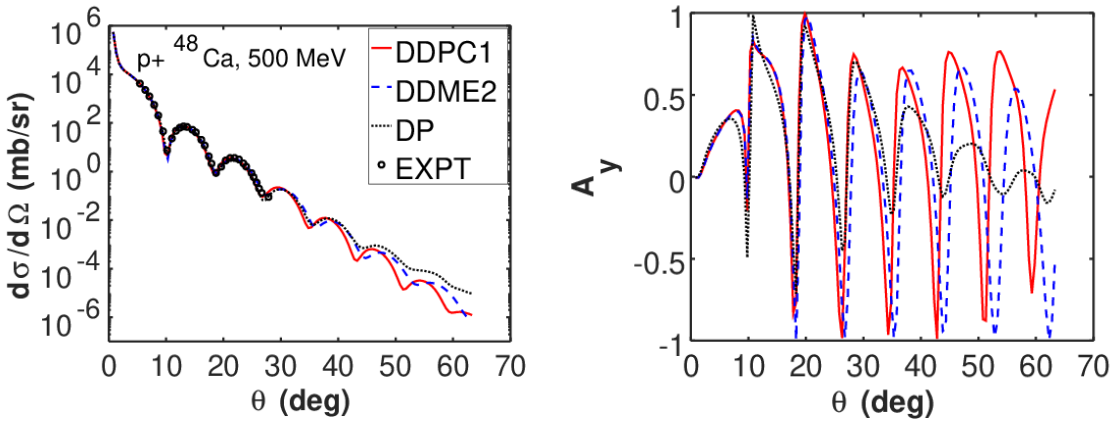

Figure 7: Same as in figure 5 but for $T_{lab} = 500$MeV.

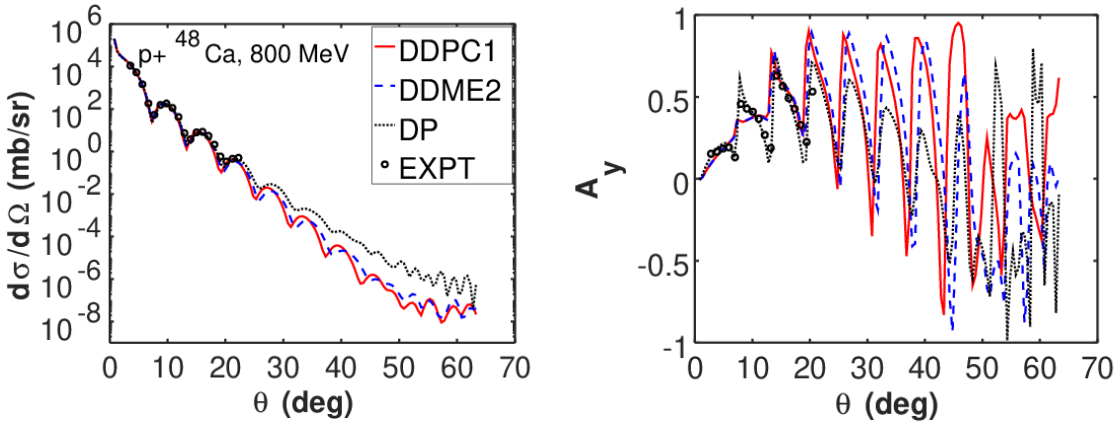

Figure 8: Same as in figure 5 but for $T_{lab} = 800$MeV.

3.3 Horowitz-Love-Franey model (HLF)

Here, we present the results of the scattering observables calculated using the Horowitz-Love-Franey model with the densities obtained via DDME2 and DDPC1 energy functionals.Figures 9 to 14 show plots of the scattering observables for proton scattering from $^{40,48,60}Ca$ calculated using Horowitz-Love-Franey model with the DDME2 and DDPC1 energy functionals. The results obtained using the Dirac phenomenology are also shown for comparison. The results of the calculations using HLF formalism with the DDME2 and DDPC1 are shown in solid and dashed lines, respectively. The DP results are shown in dotted lines while experimental data are shown

in circles. One can observe from figures 9, 10, and 11 that the HLF formalism gives very good descriptions of the scattering observables for proton scattering from ^{40,48} at energies lower than 400 MeV where the IA1 formalism failed. It should be noted that while calculating the scattering observables using HLF formalism, we have included Pauli blocking. See [2] for details. Figures 12 to 14 are predictions, as there are no available experimental data as at the time of writing this work. We hope that in future there will be scattering observable data for proton elastic scattering from ^{60}Ca at intermediate energies, which will enable us to know which of the two formalisms gives better descriptions of the differential cross section and analysing power.

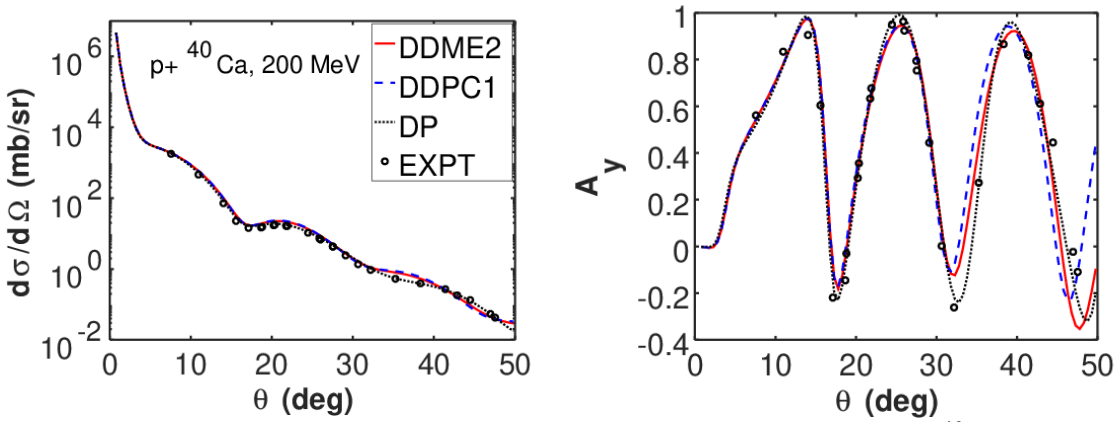

Figure 9: Differential cross-section and analysing power for proton scattering from ^{40}Ca at $T_{lab} = 200$ MeV using HLF formalism with the DDPC1 and DDME2 energy functionals. The results of the calculations using HLF formalism with the DDME2 and DDPC1 are shown in solid and dashed lines, respectively. The DP results are shown in dotted lines while experimental data are shown in circles.

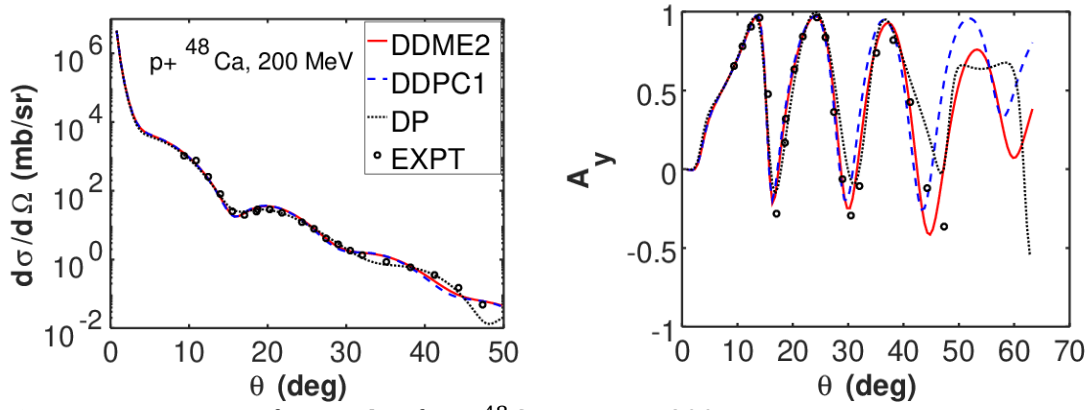

Figure 10: Same as in figure 9 but for ^{48}Ca at $T_{lab} = 200$ MeV.

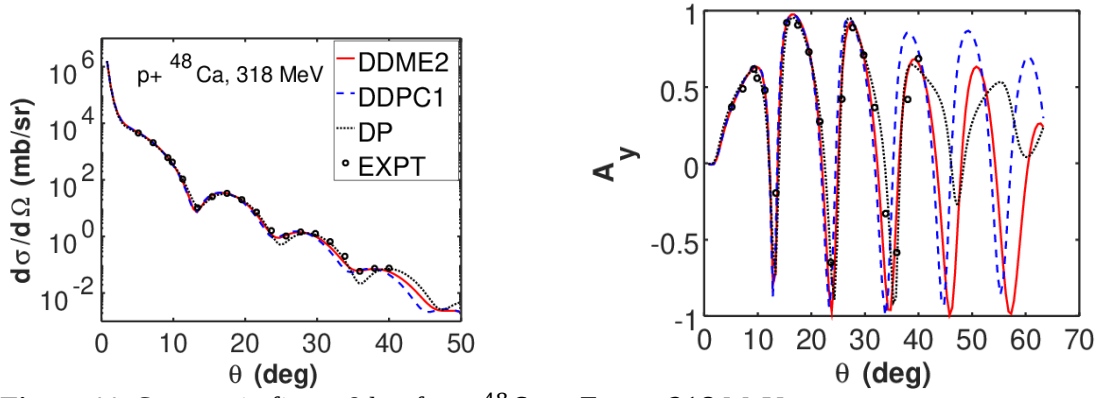

Figure 11: Same as in figure 9 but for ^{48}Ca at $T_{lab} = 318$ MeV.

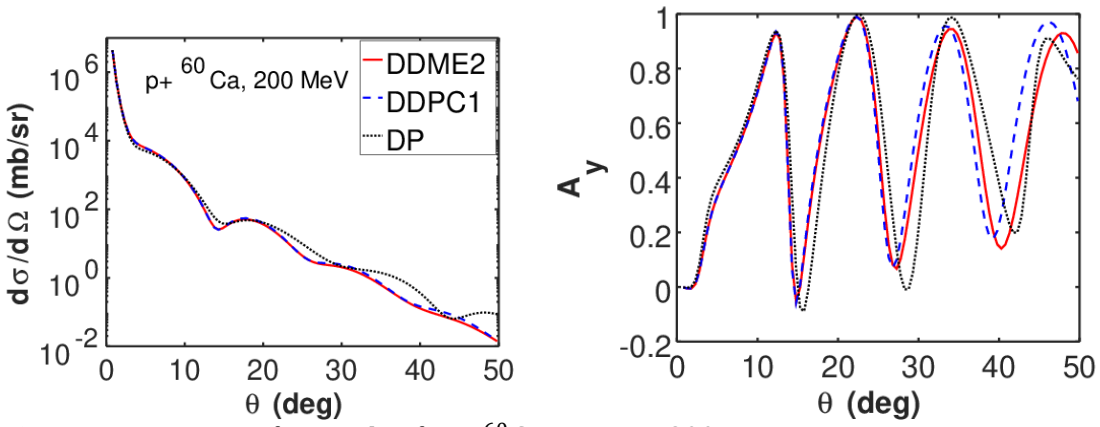

Figure 12: Same as in figure 9 but for ^{60}Ca at $T_{lab} = 200$ MeV.

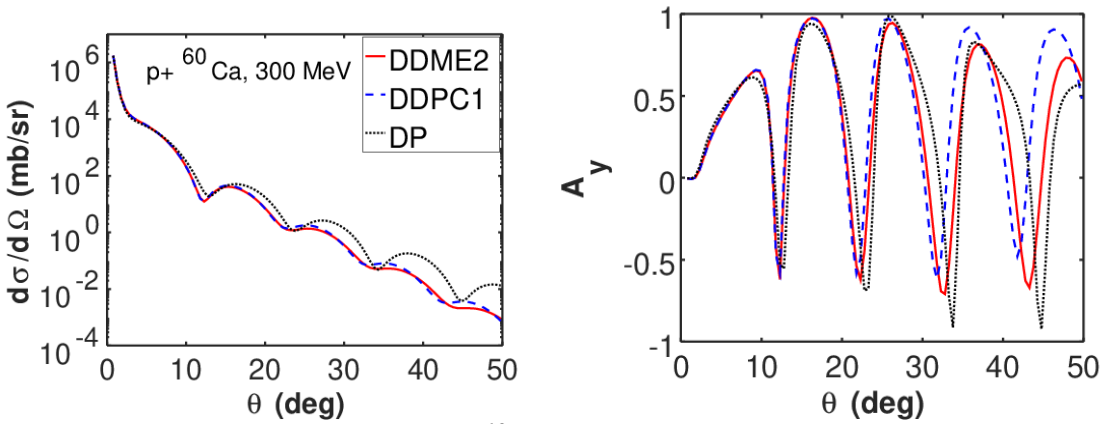

Figure 13: Same as in figure 9 but for ^{60}Ca at $T_{lab} = 300$ MeV.

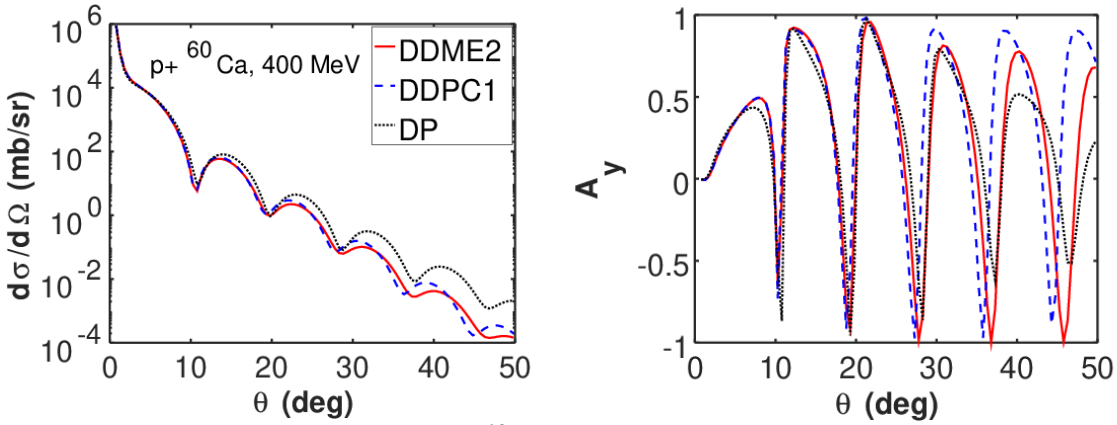

Figure 14: Same as in figure 9 but for ^{60}Ca at $T_{lab} = 400$ MeV.

4. Conclusion

We have presented calculations of scattering observables for proton elastic scattering from some calcium isotopes using the original relativistic impulse approximation (IA1) and Horowitz-Love-Franey model. We demonstrated here that the non-relativistic phenomenological optical model of Koning and Delaroche (implemented in the TALYS code) should only be reliably used for incident projectile energies less or equal to 200 MeV. This conclusion was drawn after calculating the differential cross-section and analysing power for proton scattering from ^{40}Ca at $T_{lab} = 65, 100, 200, 500$ MeV.

The calculation of the scattering observables was also carried out using the IA1 formalism. We demonstrated that the IA1 formalism gives very good descriptions of the scattering observables at energies higher than 400 MeV, while the IA1 formalism failed at energies lower than 400 MeV. The use of the densities obtained via the new energy functionals could not improve the results of the IA1 formalism at energies lower than 400 MeV.

Finally, the Horowitz-Love-Franey model was used in calculating the scattering observables for proton scattering from $^{40,48}Ca$ at incident projectile energies of 200 and 318 MeV. The HLF formalism gives very good descriptions of the scattering observables at $T_{lab} = 200$ and 318 MeV, where the IA1 formalism had failed. We made predictions for differential cross-section and analysing power for proton scattering from ^{60}Ca at incident projectile energies of 200, 300, and 400 MeV. We hope that future nuclear scattering experiment (after completion of the new radioactive ion-beam facilities) will focus on the measurement of the elastic scattering observables for ^{60}Ca at intermediate energies.

References

[1] W. A. Yahya, B. I. S. van der Ventel, B. C. Kimene Kaya, and R. A. Bark. Calculation of acomplete set of spin observables for proton elastic scattering from stable and unstable nuclei. *Phys. Rev. C*, 98:014620, Jul 2018.

[2] W. A. Yahya. *A Microscopic Description of Elastic Scattering from Unstable Nuclei within a Relativistic Framework*. PhD thesis, Stellenbosch University, 2018.

[3] N. Alamanos and A Gillibert. *Selected topics in reaction studies with exotic nuclei*, volume 651 of *Lect. Notes Phys.* Springer-Verlag, Berlin Heidelberg, 2004.

[4] K. Kaki. Relativistic impulse approximation analysis of unstable calcium isotopes: $^{60-74}$Ca. *Phys. Rev. C*, 79:064609, Jun 2009.

[5] R. F. Garcia-Ruiz, M. L. Bissell, K. Blaum, A. Ekstrom, N. Frommgen, G. Hagen, M. Hammen, K. Hebeler, J. D. Holt, G. R. Jansen, M. Kowalska, K. Kreim, W. Nazarewicz, R. Neugart, G. Neyens, W. Nortershouser, T. Papenbrock, J. Papuga, A. Schwenk, J. Simonis, K. A. Wendt,and D. T. Yordanov. Unexpectedly large charge radii of neutron-rich calcium isotopes. *Nature Physics*, 12:594–599, 2016.

[6] E. Khan, T. Suomijŕvi, Y. Blumenfeld, Nguyen Van Giai, N. Alamanos, F. Auger, E. Bauge, D. Beaumel, J.P. Delaroche, P. Delbourgo-Salvador, A. Drouart, S. Fortier, N. Frascaria, A. Gillibert, M. Girod, C. Jouanne, K.W. Kemper, A. Lagoyannis, V. Lapoux, A. Lepine-Szily, I. Lhenry, J. Libert, F. Marechal, J.M. Maison, A. Musumarra, S. Ottini-Hustache, P. Piattelli, S. Pita, E.C. Pollacco, P. Roussel-Chomaz, D. Santonocito, J.E. Sauvestre, J.A. Scarpaci, and T. Zerguerras. Proton scattering from the unstable nuclei 30s and 34ar: structural evolution along the sulfur and argon isotopic chains. experiment performed at the ganil national facility, caen, france. *Nuclear Physics A*, 694(1):103 – 131, 2001.

[7] Y. Matsuda, H. Sakaguchi, H. Takeda, S. Terashima, J. Zenihiro, T. Kobayashi, T. Murakami, Y. Iwao, T. Ichihara, T. Suda, T. Ohnishi, Y. Watanabe, H. Otsu, K. Yoneda, Y. Satou, K. Ozeki, and M. Kanazawa. Elastic scattering of protons from ^{9}c with a 290 MeV/nucleon ^{9}c beam. *Phys. Rev. C*, 87:034614, Mar 2013.

[8] P. Egelhof, G.D. Alkhazov, M.N. Andronenko, A. Bauchet, A.V. Dobrovolsky, S. Fritz, G.E. Gavrilov, H. Geissel, C. Gross, A.V. Khanzadeev, G.A. Korolev, G. Kraus, A.A. Lobodenko, G. Münzenberg, M. Mutterer, S.R. Neumaier, T. Schäfer, C. Scheidenberger, D.M. Seliverstov, N.A. Timofeev, A.A. Vorobyov, and V.I. Yatsoura. Nuclear-matter distributions of halo nuclei from elastic proton scattering in inverse kinematics. *The European Physical Journal A - Hadrons and Nuclei*, 15(1):27–33, 2002.

[9] K. Kaki. Relativistic impulse approximation analysis of elastic proton scattering from He isotopes. *Phys. Rev. C*, 89:014620, Jan 2014.

[10] B. C. Clark, S. Hama, R. L. Mercer, L. Ray, G. W. Hoffmann, and B. D. Serot. Energy dependence of the relativistic impulse approximation for proton–nucleus elastic scattering. *Phys. Rev. C*, 28:1421–1424, Sep 1983.

[11] D. P. Murdock and C. J. Horowitz. Microscopic relativistic description of proton- nucleusscattering. *Phys. Rev. C*, 35:1442–1462, Apr 1987.

[12] C. J. Horowitz, D. P. Murdock, and B. D. Serot. *Computational Nuclear Physics 1: Nuclear Structure*, chapter The Relativistic Impulse Approximation, pages 129 – 151. Springer–Verlag Berlin Heidelberg, 1991.

[13] M. Rashdan. Implication of proton-nucleus scattering for density distributions of unstable nuclei. *Eur. Phys. J. A*, 16:371–379, 2003.

[14] L. Ray and G. W. Hoffmann. Relativistic and nonrelativistic impulse approximation descriptions of 300 – 1000 MeV proton nucleus elastic scattering. *Phys. Rev. C*, 31:538–560, Feb 1985.

[15] L. Ray, G.W. Hoffmann, and W.R. Coker. Nonrelativistic and relativistic descriptions of proton-nucleus scattering. *Physics Reports*, 212(5):223 – 328, 1992.

[16] J. A. McNeil, L. Ray, and S. J. Wallace. Impulse approximation NN amplitudes for proton-nucleus interactions. *Phys. Rev. C*, 27:2123–2132, May 1983.

[17] C. J. Horowitz. Relativistic love–franey model: Covariant representation of the nn interaction for n–nucleus scattering. *Phys. Rev. C*, 31:1340–1348, Apr 1985.

[18] J. A. McNeil, J. R. Shepard, and S. J. Wallace. Impulse–approximation dirac optical potential. *Phys. Rev. Lett.*, 50:1439–1442, May 1983.

[19] Z. P. Li, G. C. Hillhouse, and J. Meng. Validity of the relativistic impulse approximation for elastic proton-nucleus scattering at energies lower than 200 MeV. *Phys. Rev. C*, 78:014603, 2008.

[20] T. Niksic, D. Vretenar, and P. Ring. Relativistic nuclear energy density functionals: Mean-field and beyond. *Progress in Particle and Nuclear Physics*, 66(3):519 – 548, 2011.

[21] B. G. Todd-Rutel and J. Piekarewicz. Neutron–rich nuclei and neutron stars: A new accurately calibrated interaction for the study of neutron–rich matter. *Phys. Rev. Lett.*, 95:122501, Sep 2005.

[22] I. Angeli and K.P. Marinova. Table of experimental nuclear ground state charge radii: An update. *Atomic Data and Nuclear Data Tables*, 99(1):69 – 95, 2013.

[23] A.J. Koning and J.P. Delaroche. Local and global nucleon optical models from 1 kev to 200 MeV. *Nuclear Physics A*, 713(3):231 – 310, 2003.

[24] S. Hama, B. C. Clark, E. D. Cooper, H. S. Sherif, and R. L. Mercer. Global dirac optical potentials for elastic proton scattering from heavy nuclei. *Phys. Rev. C*, 41:2737, 1990.

[25] E. D. Cooper, S. Hama, B. C. Clark, and R. L. Mercer. Global dirac phenomenology for proton-nucleus elastic scattering. *Phys. Rev. C*, 47:297, 1993.

[26] A.J. Koning, D. Rochman, and S.C. van der Marck. Extension of talys to 1 GeV. *Nuclear Data Sheets*, 118:187 – 190, 2014.